THE JOURNAL OF PHYSICAL CHEMISTRY C

pubs.acs.org/JPCC Article

Full Visible Spectrum Panchromatic Triple Donor Dye for Dye-Sensitized Solar Cells

Jonathon Watson, Taylor J. Santaloci, Hammad Cheema, Ryan C. Fortenberry, and Jared H. Delcamp*

Cite This: J. Phys. Chem. C 2020, 124, 25211−25220 Read Online

ACCESS | Metrics & More | Article Recommendations | Supporting Information

ABSTRACT: An organic dye with three electron donating groups is studied that has broad full visible spectrum panchromatic absorption in solution. The donor groups introduce six significant optical transitions spaced throughout the visible spectrum to give a dye with near uniform molar absorptivity across the visible spectrum. This unique material is characterized by optical, electrochemical, and computational methods. Within dye-sensitized solar cell (DSC) devices, this material shows a strong photocurrent output of ∼20 mA/cm^2 with no cosensitization. DSC devices are characterized through impedance spectroscopy, current−voltage curve analysis, and incident photon-to-current conversion efficiency measurements. Importantly, minimal DSC device performance loss is observed after 500 h of continuous irradiation.

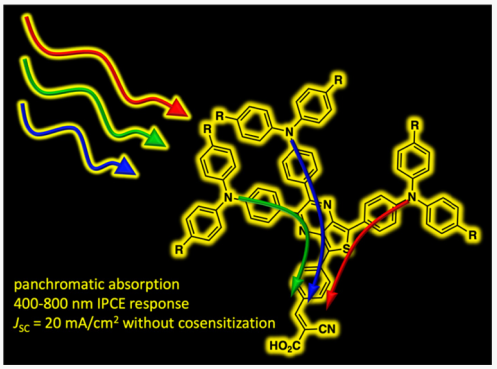

INTRODUCTION

Dye-sensitized solar cells (DSCs) provide an attractive alternative energy technology with a low cost of fabrication, tunability, and remarkable performance under low light conditions.[1−6] n-Type DSC devices operate by the photoexcitation of a sensitizer to induce electron transfer to a semiconductor (typically TiO_2). The electron then traverses an external circuit before being collected by a redox shuttle (RS) at the counter electrode and returned to the oxidized sensitizer to complete the circuit. The dye plays a critical role in light harvesting, and a strong panchromatic photoresponse throughout the visible region into the near-infrared (NIR) region of the solar spectrum is needed to avoid solar energy waste.[7,8]

The design of a single chromophore to collect all of the photons throughout the visible solar spectrum and into the NIR region is a long-standing challenge for organic dyes (Figure 1).[8,9] The pursuit of cosensitization strategies with multiple chromophores is common to avoid weakly absorbing regions of the solar spectrum. While this is an effective strategy for maximizing the device power conversion efficiency (PCE),[6,10−20] the optimization of the device can be non-trivial with several different approaches possible. These approaches include the use of cocktail solutions, sequential dye depositions, and covalently linking chromophores.[21−23] Additionally, finding structurally compatible chromophores, elucidating spectroscopically compatible chromophores, and reassessing the need for deaggregation agents at the TiO_2 surface add additional opportunities for improving PCE values at the expense of lengthier optimizations. To address these discovery rate slowing issues, a triple donor dye design strategy is put forward in this manuscript, which gives a fully panchromatic dye throughout the visible spectrum (Figure 1).

Thienopyrazine (TPz)-based dyes are well known in the DSC literature owing to appreciable NIR absorption in many cases.[8,24−27] NIR region access is partly made possible due to the proaromatic nature of the TPz group when intramolecular charge transfer (ICT) occurs from donor to acceptor substituents across the TPz thiophene.[28,29] However, most ICT dyes exhibit a single strong broad band collecting low-energy photons with a significant loss of absorbance in the higher-energy region (Figure 1).[28] Designing higher-energy absorption bands into chromophores can allow for the collection of these higher-energy photons to improve DSC device performances.[30] TPz dyes open additional synthetically accessible substitution sites on the pyrazine ring cross-conjugated with the donor and acceptor substituted on the thiophene ring.[31−33] The addition of higher-energy ICT pathways via cross-conjugation can be used to fill in the absorption spectrum gaps to give a single dye that absorbs across the full spectrum. The addition of two triarylamine (TAA) donor groups on the TPz ring to give the triple donor dye **JW1** for comparison with the single donor dye **NL6** is attractive since the TPz dye excited states are often low in energy, which can harm charge injection efficiencies into

Received: July 31, 2020
Revised: October 21, 2020
Published: November 9, 2020

https://dx.doi.org/10.1021/acs.jpcc.0c07003
J. Phys. Chem. C 2020, 124, 25211−25220

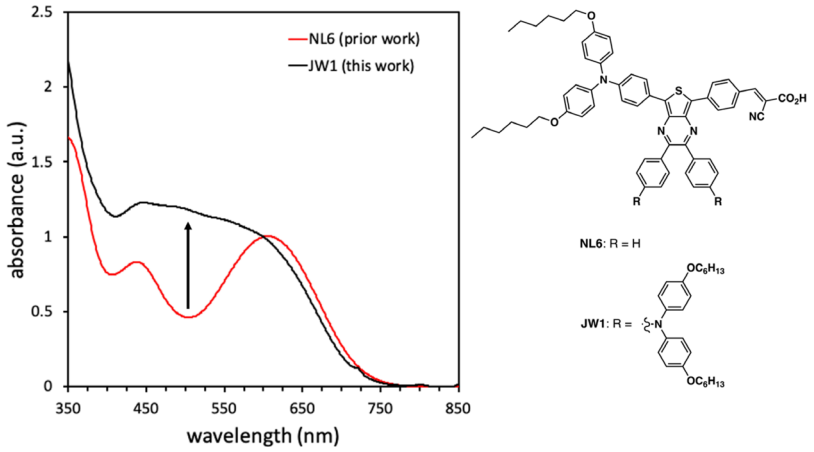

Figure 1. Absorption spectra in dichloromethane of **NL6** (top) with a characteristic electronic structure for traditional organic intramolecular charge transfer (ICT) dyes and **JW1** (bottom), which shows true panchromatic absorption as a result of the unique triple donor design. The *y* axis values are normalized at 600 nm.

Scheme 1. Synthetic Route to JW1

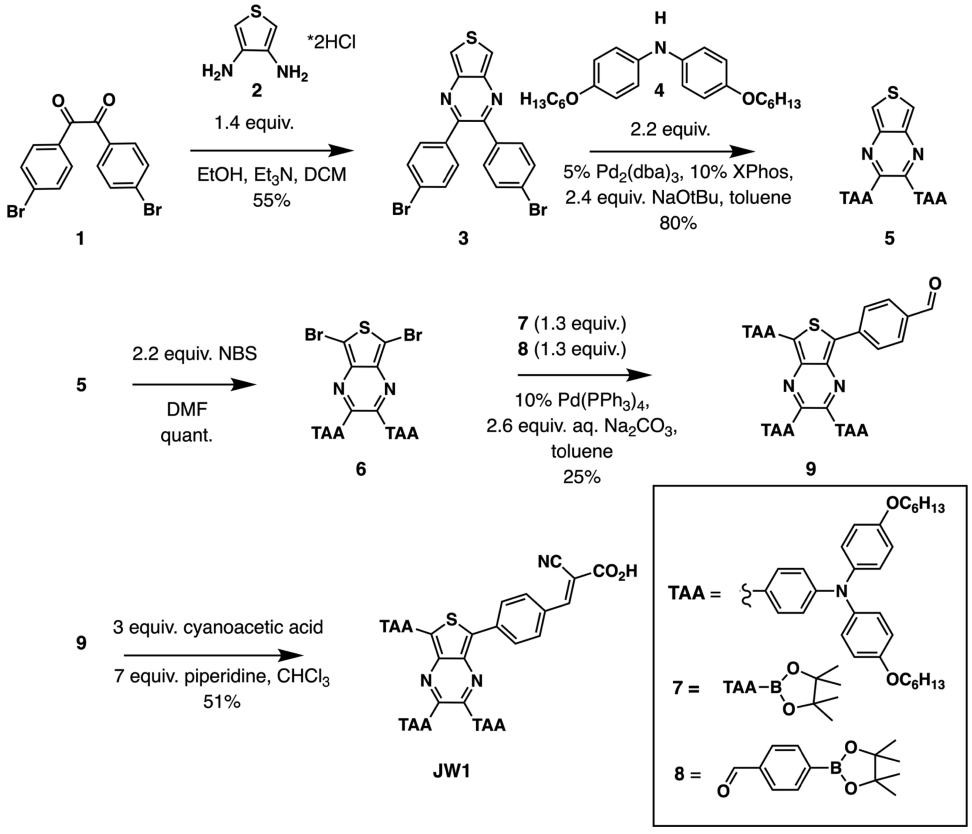

TiO_2.[26,28] Addition of donor functionality to the electron-deficient TPz ring increases the electron density on the TPz ring, which can increase the excited-state energy to allow for more efficient electron injections into TiO_2.

EXPERIMENTAL SECTION

General Information. All commercially obtained reagents were used as received. Intermediates **4** and **7** shown in Scheme 1 were prepared following a literature precedent.[34] Thin-layer chromatography (TLC) was conducted with Sorbtech silica XHL TLC plates and visualized with UV light. Column chromatography was performed using Sorbent Tech P60, 40–63 μm (230 × 400 mesh). ^{1}H NMR spectra were recorded on a Bruker Avance-300 (300 MHz) spectrometer. Data reported as s = singlet, d = doublet, t = triplet, q = quartet, p = pentet, m = multiplet, br = broad, ap = apparent, and dd = doublet of doublets; coupling constant(s) in Hz; integration. Absorbance spectra were measured with a Cary 5000 UV–vis–NIR spectrophotometer with a dichloromethane solution. Cyclic voltammetry curves were measured with a C–H Instruments electrochemical analyzer (Model CHI602E). Measurements were taken using a platinum counter electrode, an Ag/AgCl reference electrode, and a glassy carbon working electrode. The electrolytic solvent used was 0.1 M Bu_4NPF_6 in

https://dx.doi.org/10.1021/acs.jpcc.0c07003
J. Phys. Chem. C 2020, 124, 25211–25220

dichloromethane. Ferrocene was used as a reference standard and taken as 0.70 V versus the NHE in DCM. Oxidation potentials are reported versus the normal hydrogen electrode (NHE) in dichloromethane.

Synthetic Protocols for JW1. *2,3-Bis(4-bromophenyl)-thieno[3,4-b]pyrazine (**3**, See Scheme 1 for Numbered Structures).* To a 500 mL round-bottomed flask, 4,4′-dibromobenzil **1** (2.24 g, 6.09 mmol), 3,4-diaminothiophene dihydrochloride **2** (1.6 g, 8.51 mmol), ethanol (51 mL, 0.12 M), and dichloromethane (51 mL, 0.12 M) were added. After purging with N_2 for 20 min, triethylamine (27 mL, 0.23 M) was added, and the mixture was sealed and allowed to stir at 50 °C for 18 h. The mixture was then extracted with 1:1 dichloromethane/water (100 mL) three times and dried over Na_2SO_4. After the removal of solvent under reduced pressure, the crude mixture was subjected to a silica gel column for purification with 20% dichloromethane/hexanes as the eluent, and a yellow crystalline solid was isolated (1.5 g, 3.36 mmol, 55% yield). ^{1}H NMR (300 MHz, $CDCl_3$) δ 8.06 (s, 2H), 7.48 (d, J = 8.5 Hz, 4H) 7.31 (d, J = 8.5 Hz, 4H) ppm. ^{13}C NMR (75 MHz, $CDCl_3$) δ 151.9, 141.6, 137.9, 131.7, 131.4, 123.9, 118.1 ppm. IR (neat, cm^{-1}) 3076, 3057, 2971, 2918, 1672, 1587, 1484, 1391, 1357, 1282, 1280. HRMS ESI (positive mode) m/z calcd for $C_{18}H_{10}Br_2N_2S$ $[M]^+$: 446.8990, found 446.9017.

*4,4′-(Thieno[3,4-b]pyrazine-2,3,-diyl)bis(N,N-bis(4-hexyloxy)phenyl)aniline) (**5**).* To a flame dried 50 mL round-bottomed flask, intermediate **3** (1.5 g, 3.36 mmol), compound **4**[34] (2.7 g, 7.31 mmol), and toluene (15 mL, 0.25 M) were added, and the mixture was purged with N_2 for 20 min. Sodium *tert*-butoxide (775 mg, 8.07 mmol), XPhos (160 mg, 0.34 mmol), and $Pd_2(dba)_3$ (154 mg, 0.17 mmol) were then added in one portion, and the reaction was sealed and stirred at 100 °C for 12 h. The product was extracted three times with 100 mL 1:1 dichloromethane/water. The organic phase was dried with Na_2SO_4, and the solvent was removed under reduced pressure. The crude product was purified by silica gel column chromatography with 30% dichloromethane/hexanes as the eluent, affording an orange oil (2.76 g, 2.69 mmol, 80% yield). ^{1}H NMR (300 MHz, $CDCl_3$) δ 7.91 (s, 2H), 7.31 (d, J = 8.5 Hz, 4H), 7.09 (d, J = 8.7 Hz, 8H), 6.85 (ap d, J = 11.7 Hz, 12 H), 3.96 (t, J = 6.5 Hz, 8H), 1.84−1.73 (m, 8H), 1.53−1.29 (m, 24H), 0.93 (t, J = 6.8 Hz, 12H) ppm. ^{13}C NMR (75 MHz, $CDCl_3$) δ 155.9, 153.5, 149.5, 141.7, 140.2, 130.8, 130.6, 127.1, 118.9, 116.5, 115.3, 68.3, 31.7, 29.4, 25.9, 22.7, 14.1 ppm. IR (neat, cm^{-1}) 2927, 2855, 2545, 2440, 2158, 2013, 1975, 1715, 1599, 1503, 1468, 1318, 1288, 1280, 1167. HRMS ESI (positive mode) m/z calcd for $C_{66}H_{78}N_4O_4S$ $[M]^+$: 1023.5822, found 1023.5820.

*4,4′-(5,7-Dibromothieno[3,4-b]pyrazine-2,3,-diyl)bis(N,N-bis(4-hexyloxy)phenyl)aniline) (**6**).* To a 100 mL round-bottomed flask, intermediate **5** (1.5 g, 1.46 mmol) and *N*,*N*-dimethylformamide (41 mL, 0.036 M) were added. The solution was allowed to stir at 0 °C for 10 min and then *N*-bromosuccinimide (2.2 equiv, 0.573 g, 3.22 mmol) was added to the reaction flask at 0 °C and allowed to stir at room temperature. After 5 h, the reaction mixture was extracted with 1:1 dichloromethane/water (100 mL) two times. The organic phase was dried with Na_2SO_4, and the solvent was removed under reduced pressure. The crude product was purified by filtration through a pad of silica gel with dichloromethane as the eluent, affording a red oil (1.7 g, 1.44 mmol, quantitative yield). ^{1}H NMR (300 MHz, $CDCl_3$) δ 7.35 (d, J = 8.2 Hz, 4H), 7.08 (d, J = 8.2 Hz, 8H), 6.84 (m, 12H), 3.95 (t, J = 6.0 Hz, 8H), 1.85−1.61 (m, 8H), 1.55−1.19 (m, 24H), 0.92 (t, J = 6.4 Hz, 12H) ppm. ^{13}C NMR (75 MHz, $CDCl_3$) δ 156.1, 154.7, 150.0, 139.9, 139.3, 130.9, 129.6, 127.4, 118.3, 115.4, 103.5, 68.3, 31.7, 29.4, 25.9, 22.7, 14.1 ppm. IR (neat, cm^{-1}) 2919, 2852, 2348, 1596, 1503, 1466, 1237. HRMS ESI (positive mode) m/z calcd for $C_{66}H_{76}Br_2N_4O_4S$ $[M]^+$: 1178.3954, found 1178.3928.

*4-(2,3,7-Tris(4-(bis(4-hexyloxy)phenyl)amino)phenyl)-thieno[3,4-b]pyrazin-5-yl)benzaldehyde (**9**).* To a pressure flask, intermediate **6** (0.40 g, 0.34 mmol), **7** (1.3 equiv, 0.25 g, 0.44 mmol),[34] **8** (1.3 equiv, 0.10 g, 0.44 mmol), 2.0 M aqueous sodium carbonate solution (0.50 mL, 1.3 M), toluene (2.0 mL, 0.25 M), and two drops of Aliquat 336 were added. The mixture was then purged with N_2 for 20 min before adding $Pd(PPh_3)_4$ (0.039 g, 0.034 mmol). The reaction was sealed and stirred at 100 °C for 12 h. The crude product was isolated by extraction with 1:1 dichloromethane/water (20 mL) three times. The organic phase was dried over Na_2SO_4, and the solvent was removed under reduced pressure. The compound was purified by silica gel column chromatography and eluted with a 50% dichloromethane/hexane mixture to afford a purple solid (0.13 g, 0.085 mmol, 25% yield). ^{1}H NMR (300 MHz, $CDCl_3$) δ 9.99 (s, 1H), 8.48 (d, J = 8.3 Hz, 2H), 8.10 (d, J = 8.8 Hz, 2H), 7.92 (d, J = 8.3 Hz, 2H), 7.47−7.35 (m, 4H), 7.11 (ap t, J = 7.6 Hz, 12H), 6.98 (d, J = 8.9 Hz, 2H), 6.90−6.78 (m, 16H), 3.95 (t, J = 6.4 Hz, 12H), 1.85−1.61 (m, 12H), 1.55−1.19 (m, 36H), 0.92 (t, J = 6.7 Hz, 18H) ppm. ^{13}C NMR (75 MHz, $CDCl_3$) δ 156.2, 156.0, 156.0, 153.3, 152.2, 149.9, 149.6, 149.0, 140.6, 140.3, 140.3, 140.2, 140.0, 138.4, 134.2, 130.9, 130.8, 130.7, 130.4, 128.8, 127.5, 127.4, 127.2, 125.2, 120.0, 118.6, 118.3, 115.5, 115.4, 68.4, 31.8, 29.5, 25.9, 22.8, 14.2 ppm. IR (neat, cm^{-1}) 2956, 2924, 2856, 2332, 1712, 1639, 1536, 1456, 1412, 1389, 1241, 1165. HRMS ESI (positive mode) m/z calcd for $C_{103}H_{119}N_5O_7SCs$ $[M + Cs]^+$: 1702.7885, found 1702.7983.

*(E)-2-Cyano-3-(4-(2,3,7-tris(4-(bis(4-hexyloxy)phenyl)-amino)phenyl)thieno[3,4-b]pyrazin-5-yl)phenyl)acrylic Acid (**JW1**).* Compound **9** (0.040 g, 0.025 mmol) was dissolved in $CHCl_3$ (2.5 mL, 0.01 M), cyanoacetic acid (7.0 mg, 0.075 mmol), and piperidine (15.0 mg, 0.18 mmol) under N_2. The reaction was heated to 80 ° C in a sealed vial and stirred for 5 h. The reaction was acidified using AcOH (5 mL) and diluted with diethyl ether (30 mL). Excess AcOH was removed by washing with H_2O (30 mL) three times. After removal of the solvent under reduced pressure, the crude mixture was subjected to a filtration plug with alumina for purification with 5% methanol/dichloromethane as the eluent, and purple solid was isolated after evaporation (21 mg, 0.013 mmol, 51% yield). ^{1}H NMR (300 MHz, $CDCl_3$) δ 8.48 (br d, 2H), 8.30 (s, 1H), 8.10 (s, 4H), 8.05−7.90 (m, 4H), 7.49 (m, 2H), 7.12−7.05 (m, 10H), 7.05−6.90 (m, 2H), 6.90−6.75 (m, 16H), 3.94 (br s, J = 5.5 Hz, 12H), 1.78 (ap br s, 12H), 1.50−1.10 (m, 36H), 1.00−0.80 (m, 18H) ppm. IR (neat, cm^{-1}) 3479, 3087, 2924, 2851, 2683, 2336, 2335, 1693, 1594, 1467, 1238. HRMS ESI (negative mode) m/z calcd for $C_{106}H_{120}N_6O_8SCs$ $[M + Cs]^+$: 1769.7955, found 1769.7939.

Device Fabrication. Chenodeoxycholic acid (CDCA) was purchased from Chem-Impex International. TEC 10 and TEC 7 glass were purchased from Hartford Glass. For the photoanode, TEC 10 glass was cut into 2 × 2 cm^2 squares, and then the substrates were submerged in a 0.2% Deconex 21 aqueous solution and sonicated for 15 min at room

https://dx.doi.org/10.1021/acs.jpcc.0c07003
J. Phys. Chem. C 2020, 124, 25211−25220

temperature. The electrodes were rinsed with water and sonicated in acetone for 10 min followed by sonication in ethanol for 10 min. Finally, the electrodes were placed under UV/ozone for 15 min (UV-Ozone Cleaning System, Model ProCleaner by UVFAB Systems). A compact TiO_2 underlayer is then applied by treatment of the substrate submerged in a 40 mM $TiCl_4$ solution in water (carefully prepared from 99.9% $TiCl_4$ between 0 and 5 °C with slow addition). The submerged substrates (conductive side up) were heated for 30 min at 70 °C. After heating, the substrates were rinsed first with water and then with ethanol. The photoanode consists of thin TiO_2 electrodes composed of a 10 μm mesoporous TiO_2 layer (particle size, 20 nm, Dyesol, DSL 18NR-T) and a 5.0 μm TiO_2 scattering layer (particle size, 100 nm, Solaronix R/SP). All of the layers were screen printed from a Sefar screen (54/137−64 W). Between each print, the substrate was heated for 7 min at 125 °C and the thickness was measured with a profilometer (Alpha-Step D-500 KLA Tencor). After all layers were deposited, the substrate was then sintered with progressive heating from 125 °C (5 min ramp from r.t., 5 min hold) to 325 °C (15 min ramp from 125 °C, 5 min hold) to 375 °C (5 min ramp from 325 °C, 5 min hold) to 450 °C (5 min ramp from 375 °C, 15 min hold) to 500 °C (5 min ramp from 450 °C, 15 min hold) using a programmable furnace (Vulcan 3-Series Model 3-550). The cooled sintered photoanode was soaked for 30 min at 70 °C in a 40 mM $TiCl_4$ water solution and heated again at 500 °C for 30 min prior to sensitization. The complete working electrode was prepared by immersing the TiO_2 film into the dye solution for 16 h. The solution for the best performing device is 0.3 mM dye in a chloroform:ethanol mixture (3:7) though other solvents were investigated, as shown in Figures S4−S7. The dye:CDCA molar ratio for the optimized devices of **JW1** is 1:10. For preparing counter electrodes, 2 × 2 cm^2 squares of TEC 7 FTO electrodes were pin hole drilled under water using a Dremel-4000 with Dremel 7134 Diamond Taper Point Bit from the nonconductive side to the taped FTO side. The electrodes were washed with water followed by 0.1 M HCl in EtOH and sonication in an acetone bath for 10 min. The washed FTO electrodes were then dried at 400 °C for 15 min. A thin layer of Pt-paste (Solaronix, Platisol T/SP) was slot printed on the FTO, and the printed electrodes were then cured at 450 °C for 10 min. After allowing them to cool to room temperature, the working electrodes were then sealed with a 25 μm thick hot melt film (Surlyn, Solaronix, "Meltonix 1170-25") by heating the system at 130 °C under 0.2 psi pressure for 1 min. The devices were completed by filling the electrolyte by predrilled holes in the counter electrodes, and finally, the holes were sealed with a Surlyn precut circle and a thin glass cover by heating at 130 °C under pressure 0.1 psi for 25 s. The electrolyte is 1.0 M 1,3-dimethylimidazolium iodide (DMII), 0.5 M 4-*tert*-butylpyridine (TBP), 0.03 M I_2, 0.1 M guanidinium thiocyanide (GuNCS), and 1.0 M lithium iodide (LiI) in acetonitrile:valeonitrile (85:15, v/v) solvent unless otherwise noted. Finally, soldered contacts were added with an MBR Ultrasonic soldering machine (model USS-9210) with the solder alloy (Cerasolzer wire dia. 1.6 mm item # CS186-150). A circular black mask (active area 0.15 cm^2) punched from black tape was used in the subsequent photovoltaic studies.

Device Characterization Information. *Current−Voltage Curves.* Photovoltaic characteristics were measured using a 300 W Xenon lamp (Model SF300A, SCIENCETECH Inc. Class AAA) solar simulator equipped with an AM 1.5 G filter for a less than 2% spectral mismatch. Prior to each measurement, the solar simulator output was calibrated with a KG5 filtered monocrystalline silicon NREL calibrated reference cell from ABET Technologies (Model 15150-KG5). The current density−voltage characteristic of each cell was obtained with a Keithley digital source meter (Model 2400).

The incident photon-to-current conversion efficiency was measured with an IPCE instrument manufactured by Dyenamo composed of a 175 W Xenon lamp (CERMAX, Model LX175F), a monochromator (Spectral Products, Model CM110, Czerny-Turner, dual- grating), a filter wheel (Spectral Products, Model AB301T, fitted with filter AB3044 [440 nm high pass] and filter AB3051 [510 nm high pass]), a calibrated UV-enhanced silicon photodiode reference, and Dyenamo issued software. Electrochemical impedance spectroscopy (EIS) was measured with a C-H Instruments electrochemical analyzer (Model CHI6054E) in the dark with a bias at open circuit voltages measured through $J-V$ measurements. The spectra were scanned in a frequency range of $10^{-1}-10^{5}$ Hz at room temperature. The alternating current (AC) amplitude was set at 10 mV.

Small modulation photovoltage transient measurements were carried out with the Dyenamo toolbox (DN-AE01). During measurements, the intensity of the light source is controlled by a modulating voltage on top of a bias voltage to a white LED. The open-circuit voltage response is measured multiple times and averaged. The rise and decay times are calculated with the aid of the Levenberg−Marquard curve-fitting algorithm in LabView. The carrier or the electron lifetime of the solar cell is obtained from the averaging of rise and decay times. To the base light intensity was added a small square wave modulation (<10% intensity). With the repetition frequency of 2 Hz, the modulation amplitude of 10 mV and 1000 samples/second with averages of five was employed. The option for light off after every measurement was selected, and bias voltages were 2.8, 2.85, 2.9, 2.95, and 3 V, respectively, for the LED light with the highest voltage being near 1 sun intensity throughout the spectral region being illuminated. The direction of illumination was always from the TiO_2 side, and the device was 5 cm far from the LED light source.

Charge extraction under open circuit conditions (Q_{oc}) as a function of light intensity was carried out with a Dyenamo Toolbox (DN-AE01) instrument and software. Different open-circuit values were achieved by the programmed control of a biased LED from 2.5 to 3.2 V. The intensity of the LED light source (Seoul Semiconductors, Natural White, S42182H, 450−750 nm emission) is varied to modulate the device open-circuit voltage. The LED is switched on for 1 s of illumination and then switched off for 10 s with a simultaneous switch to short-circuit conditions with a monitoring of current. The total charge is found by integrating the current measured over time. The direction of illumination was from the photoanode to the counter electrode, and the device was positioned 5 cm from the LED light source.

RESULTS AND DISCUSSION

The synthesis of **JW1** proceeds in five steps from commercial and literature reported intermediates (Scheme 1). The synthetic route begins with a condensation reaction between dibromobenzil **1** and 3,4-diaminothiophene dihydrochloride **2** in the presence of triethylamine to give the TPz bridge in 55%

https://dx.doi.org/10.1021/acs.jpcc.0c07003
J. Phys. Chem. C 2020, 124, 25211−25220

yield. TPz **3** was then coupled with bis(hexyloxyaryl)amine **4**[34] under Buchwald amination conditions to yield compound **5** in 80% yield. An *N*-bromosuccinimide (NBS) bromination was then employed to install bromine groups on TPz **6** in quantitative yield. As previously observed during the synthesis of **NL6**, the selective monoaryl functionalization of TPz **6** with either the TAA donor **7** or benzaldehyde **8** yielded only the diarylated product under Suzuki conditions irrespective of the ratio of coupling partners used.[28] Instead, TPz **6** was desymmetrized via a one pot Suzuki coupling with TAA boronic ester **7**[34] and benzaldehyde boronic ester **8** to give TPz **9** in 25% yield. Finally, a Knoevenagel condensation was employed to afford **JW1** in 51% yield. **NL6** was prepared following the literature precedent.[28]

UV−vis−NIR absorption spectroscopy was used to evaluate the effects of adding multiple donor groups on the electronic spectrum of **JW1** relative to the single donor group dye **NL6** (Figure 2, Table 1). **JW1** has a uniquely broad and evenly

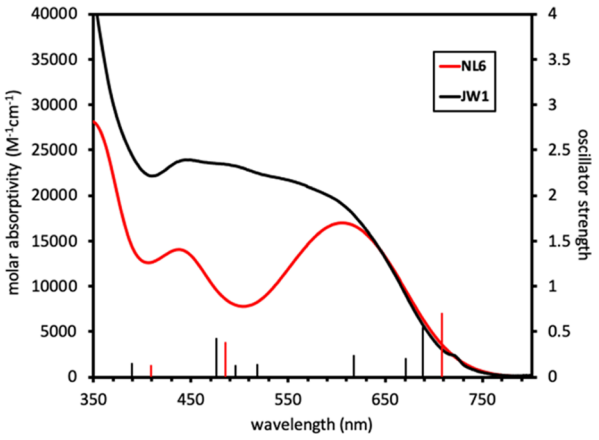

Figure 2. Absorption spectra of **NL6** and **JW1** in dichloromethane. Computed vertical transition energies are represented as vertical bars and use the secondary *y* axis on the right. The absorption curve of **NL6** has been previously reported.[28]

Table 1. Optical and Electrochemical Properties of JW1 and NL6

dye	λ_{max} (nm)	ε (M^{-1} cm^{-1})	λ_{onset} (nm)[a]	$E_{(S+/S)}$ (V)	$E_{(S+/S^*)}$ (V)[b]	E_g^{opt} (eV)[c]
NL6	605	17,000	730	0.92	−0.78	1.70
JW1	590	2100	730	0.85	−0.86	1.71

[a]The absorption onset (λ_{onset}) values were taken by drawing a line of best fit corresponding to the lowest energy transition in the absorption spectrum and extrapolating it to the crossing point of the *x* axis. [b]$E_{(S+/S^*)}$ was calculated using the equation: $E_{(S+/S^*)} = E_{(S+/S)} - E_g^{opt}$. [c]$E_g^{opt}$ was determined by the equation: E_g^{opt} = 1240 nm*eV/ λ_{onset}. **NL6** data has been previously reported.[28]

distributed absorption range covering the visible region and extending into the NIR region in dichloromethane. Approximately four evenly distributed absorption curve features are weakly distinguishable between 400 and 600 nm with a molar absorptivity (ε) of ≥20,000 M^{-1} cm^{-1} throughout this region. In the same region, **NL6** has two clear absorption curve features at 440 nm and 610 nm and a loss of absorption strength between the two peaks with a molar absorptivity minimum of 7500 M^{-1} cm^{-1} in this region. **JW1** has a maximum absorption (λ_{max}) shoulder at approximately 590 nm. The molar absorptivity at λ_{max} for **JW1** is 21,000 M^{-1} cm^{-1}, which is modestly higher than that observed for **NL6** (17,000 M^{-1} cm^{-1}) at the λ_{max} for **NL6** (605 nm). The absorption curve onset is nearly identical for **JW1** and **NL6** at approximately 730 nm. Solvatochromic absorption effects were examined with eight solvents (Figure S2). Interestingly, the lowest-energy absorption band varied dramatically with the solvent relative to the higher-energy absorption bands with DCM showing the most panchromatic solution behavior with a similar height high and low energy peaks. At the other extreme, ethanol shows the lowest intensity of the low-energy absorption band with a spectrum that shows significantly higher intensity absorption in the high-energy region. On the surface of TiO_2, **JW1** shows a slight increase in the intensity in the high-energy region relative to the low-energy region; however, panchromatic behavior is still present (Figure S3).

Density functional theory (DFT) and time-dependent (TD)-DFT computational studies at the B3LYP[35,36]/6-311G-(d,p)[37] level of theory were performed with Gaussian09[38] in isolation and in dichloromethane solvent to understand better the optical properties observed with **JW1** (see the Supporting Information for results with dichloromethane solvent: Figures S13 and S15, Table S5). Reasonable agreement is observed between the computational and experimental results, with the predicted vertical transitions being within approximately 0.3 eV of the λ_{max} for both **JW1** and benchmark **NL6** (Table 2, Figure 2). Three vertical transitions are observed in the 600−700 nm region for **JW1** that are primarily made up of the highest occupied molecular orbital (HOMO) to the lowest unoccupied molecular orbital (LUMO), HOMO-1 to LUMO, and HOMO-2 to LUMO transitions for each of the first three states, respectively (Figure 3 and Figure S12). The HOMO is located on the TAA group substituted on the thiophene ring, and the LUMO is primarily located across the cyanoacrylic acid (CAA) acceptor to the thiophene ring of the TPz ring. This separation of orbitals onto different regions of the dyes with some overlap at the π-bridge suggests that this system acts as an ICT dye. The LUMO density is spatially positioned adequate for efficient electron transfer to TiO_2 upon photoexcitation of **JW1**. The space occupied by the HOMO

Table 2. Select TD-DFT Data for JW1 and NL6 Obtained at the B3LYP/6-311G(d,P) Level of Theory

dye	state	orbitals	contribution (%)[a]	vert. trans. (nmleV)	oscillator strength
JW1	S0 → S1	HOMO→ LUMO	94%	689 | 1.80	0.5350
	S0 → S2	HOMO-1→ LUMO	95%	671 | 1.85	0.1981
	S0 → S3	HOMO-2→ LUMO	98%	617 | 2.01	0.2338
	S0 → S6	HOMO-3→ LUMO	63%	476 | 2.61	0.4198
NL6	S0 → S1	HOMO→ LUMO	97%	708 | 1.75	0.6971
	S0 → S2	HOMO-1→ LUMO	79%	485 | 2.56	0.3790

[a]Minor orbital contributions to each state are listed in the Supporting Information along with additional orbital images obtained with this method. Data from calculations including an implicit DCM model are also in the Supporting Information. The HOMO and LUMO orbitals along with the S0 → S1 vertical transition energy of **NL6** have been previously reported.[28]

https://dx.doi.org/10.1021/acs.jpcc.0c07003
J. Phys. Chem. C 2020, 124, 25211−25220

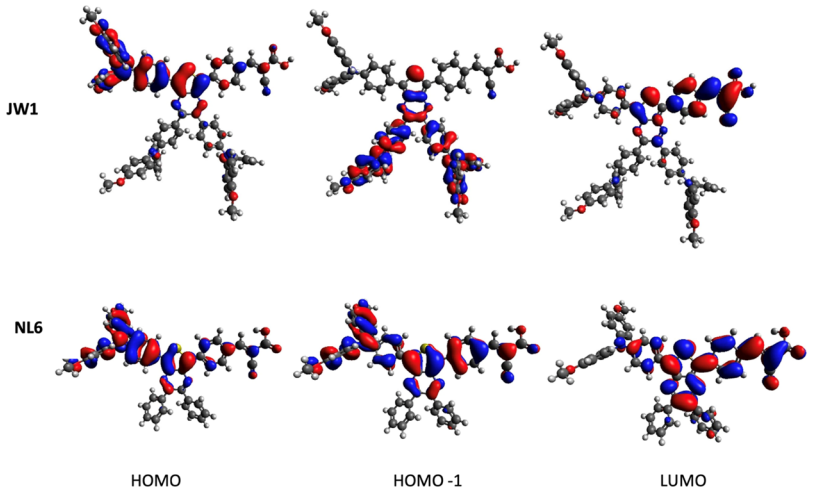

Figure 3. Select orbitals obtained at the B3LYP/6-311G(d,p) level of theory.

and the LUMO is analogous to that by **NL6** and similar in orbital energy (0.05 eV difference), which explains the near identical λ_{onset} observed for both dyes. The HOMO-1 and HOMO-2 orbitals of **JW1** are largely located on the additional two TAA groups on the pyrazine ring (Figure 3 and Figures S12 and S13). These added TAA groups result in a slightly higher vertical transition energy and aid in filling in the low molar absorptivity region of the **NL6** spectrum. Both dyes have a similar high-energy feature near 450 nm, which corresponds to an ICT event primarily from the thiophene ring with significant contributions from the TAA on the thiophene ring to the CAA acceptor region (see **NL6** HOMO-1 in Figure 3 and **JW1** HOMO-3 in Figure S12). Overall, the introduction of the three TAA donors on the TPz ring allows for cross-conjugated pathways that have enabled a true panchromatic response across the visible spectrum by introducing multiple charge transfer bands (Figure 2).

JW1 was characterized electrochemically by cyclic voltammetry in a dichloromethane solution using 0.1 M Bu_4NPF_6 as the electrolyte and ferrocene as an internal standard to evaluate the free energies of electron transfers with a DSC device (Table 1, Figure 4 and Figure S1). The ground-state oxidation potential ($E_{(S+/S)}$) for **JW1** at 0.85 V versus the normal hydrogen electrode (NHE) is less positive than **NL6** at 0.92 V versus the NHE. The less-positive $E_{(S+/S)}$ value is rationalized as the added donor groups on **JW1**, leading to a more easily oxidized dye. The thermodynamic driving force for dye regeneration (ΔG_{reg}) is therefore favorable by 500 mV for the I_3^-/I^- RS generally taken at 0.35 V versus the NHE.[21,39−42] However, it should be noted that the I_3^-/I^- RS system is complex and a single number representation is a crude estimate.[43,44] The excited-state oxidation potential ($E_{(S+/S^*)}$) of **JW1** was found to be −0.86 V versus the NHE as calculated using the equation $E_{(S+/S^*)} = E_{(S+/S)} - E_g^{opt}$, where E_g^{opt} is the optical energy gap. This suggests that the free energy for electron injection (ΔG_{inj}) into the conduction band (CB) of TiO_2 is also favorable at 360 mV when the TiO_2 CB is taken at −0.50 V versus the NHE.[41,42,45,46] Thus, the energetic values as measured by CV suggest that **JW1** is well-suited to function efficiently in DSC devices with TiO_2 and I_3^-/I^-. Notably, the excited-state oxidation potential of **JW1** is more negative than **NL6** (−0.78 V), which is due to the added electron density from the two extra amine groups on **JW1**. The more negative excited-state oxidation potentials result in a more thermodynamically favorable electron transfer to TiO_2.

DSC devices of **JW1** and **NL6** were compared via current density versus voltage ($J-V$) measurements with the PCE calculated according to the equation: $\text{PCE} = \frac{J_{SC} \times \text{FF} \times V_{OC}}{I_0}$, where J_{SC} is the short-circuit current density, FF is the fill factor, V_{OC} is the open circuit voltage, and I_0 is the intensity of incident light set to 1 sun at AM 1.5G for these studies unless otherwise noted (Figure 5 and Table 3). A J_{SC} of 19.7 mA/cm^2 was obtained for **JW1**, which is a significant increase over that obtained with **NL6** at 13.6 mA/cm^2 under identical device conditions. Analysis of the IPCE reveals that **JW1** has both a

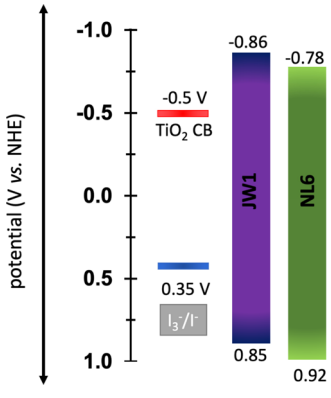

Figure 4. Energy-level diagram for **JW1** and **NL6**.

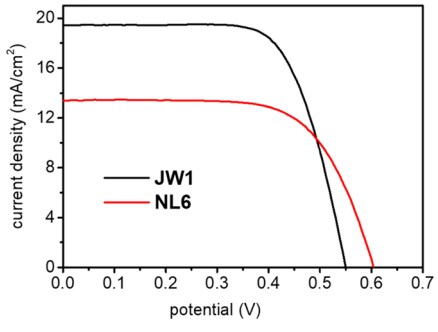

Figure 5. $J-V$ curve for **JW1** and **NL6**.

https://dx.doi.org/10.1021/acs.jpcc.0c07003
J. Phys. Chem. C 2020, 124, 25211−25220

Table 3. Summary of DSC Device Data for JW1 and NL6

dye	J_{sc} (mA/cm^2)	V_{OC} (mV)	FF (%)	PCE (%)	IPCE at 700 nm (%)
JW1	19.7	551	69	7.4	80
JW1[a]	2.3	498	78	9.2	
NL6	13.6	606	61	5.4	60

[a]Measured at 10% sun intensity. **NL6** data has been previously reported in DSC devices at 7.1% PCE (17.6 mA/cm^2) when no CDCA is added to the sensitization solution.[28] Addition of CDCA to the sensitization solvent was found to give optimal device performances with **JW1** (Figures S6 and S7). **JW1** devices give 13.0 mA/cm^2 without CDCA and 19.7 mA/cm^2 with CDCA in the sensitization solvent.

higher peak incident photon-to-current conversion efficiency (IPCE) value (80%) and no dips in the spectrum from 400 to 750 nm (Figure 6). This is significantly different from **NL6,**

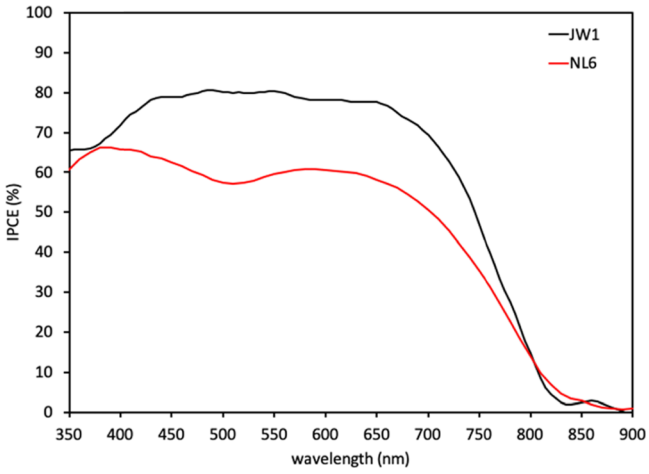

Figure 6. IPCE spectrum for **JW1** and **NL6**.

which has a peak IPCE of 65% and a local minimum in the spectrum near 500 nm. The improvement in the IPCE spectrum shape is a direct result of the panchromatic absorbance of **JW1**. A broad fully filled IPCE spectrum area such as that observed in this case is often only possible with multisensitizer devices. Thus, the introduction of high-energy absorption bands has led to a single dye with a full visible spectrum IPCE response reaching 800 nm without any significant local minima. The increased peak IPCE value is attributed to the higher energy $E_{(S+/S^*)}$ value enhancing the electron injection efficiency of photoexcited **JW1** to TiO_2. Overall, the use of a triple donor, cross-conjugated approach with **JW1** has produced a dramatic improvement of photocurrent to 19.7 mA/cm^2 from 13.6 mA/cm^2 with a traditional single donor dye structure.

A 55 mV higher photovoltage is observed with **NL6** when compared to **JW1** in identical DSC devices. To understand this difference, electrochemical impedance spectroscopy (EIS) measurements were undertaken with a fitted circuit shown on the Bode plot in Figure 7 (Table 4). The Nyquist plot shows two semicircles, with the small semicircle at low resistance being attributed to the electron transfer from the platinum counter electrode to the RS (R_{CE}). The larger, higher resistance semicircle is attributed to the nondesirable transfer of electrons from the TiO_2 surface to the electrolyte (R_{rec}). Both devices show a very similar R_{CE} value as expected;

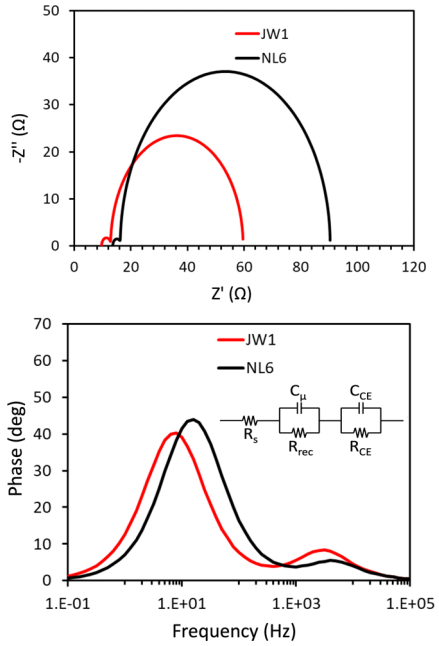

Figure 7. Nyquist (top) and Bode (bottom) plot for **JW1** and **NL6**.

Table 4. Electrochemical Impedance Spectroscopy Data

device	R_s[a] (Ω)	R_{rec} (Ω)	C_μ (mF)[b]	R_{CE} (Ω)	C_{CE} (mF)[c]	η_{cc} (%)	τ_{TiO_2} (ms)
JW1	10	47	9.9×10^{-4}	3	1.9×10^{-5}	94	10
NL6	14	74	3.3×10^{-4}	3	1.4×10^{-5}	96	20

[a]R_s is the series resistance. [b]C_μ chemical capacitance for charge accumulation in TiO_2. [c]C_{CE} is the capacitance at the electrolyte-counter electrode interface.

however, a significantly lower R_{rec} is observed for **JW1**. This indicates that the undesirable charge recombination of electrons in TiO_2 to the electrolyte is a lower resistance pathway for **JW1** DSC devices relative to **NL6**. Dye loading density studies show that **JW1** and **NL6** have similar loadings (1.0×10^{-7} mol/cm^2 vs 1.1×10^{-7} mol/cm^2, respectively). It should be noted that **JW1** is a significantly larger dye than **NL6** at the TPz bridge portion with two additional donor groups (22 Å vs 10 Å, respectively, Figures S16 and S17). Thus, the slight difference in loading is likely offset by the larger footprint of **JW1**, although the exact surface orientation of the dyes is not known and could have a significant impact on the area of TiO_2 exposed to the electrolyte. The lower R_{rec} for **JW1** leads to a modestly lower charge collection efficiency (η_{cc}) according to the equation $\eta_{cc} = 1/(1 + (R_{CE}/R_{rec}))$ for **JW1** (94%) in comparison with **NL6** (96%). The lower η_{cc} of **JW1** contributes to the IPCE being lower than the practical upper limit of 90% when accounting for reflection losses. Similarly, the Bode plot from EIS measurements allows for the analysis of electron lifetimes in TiO_2 (τ_{TiO_2}) by analyzing the peak position in the low-frequency region according to the equation $\tau_{TiO_2} = 1/(2\pi f)$, where f is the peak frequency from the Bode plot for the lower frequency peak near 10 Hz. These results show a significantly longer τ_{TiO_2} value for **NL6** of 20 ms relative to **JW1** at 10 ms, which again suggests better TiO_2 surface insulation from the electrolyte by **NL6**.

https://dx.doi.org/10.1021/acs.jpcc.0c07003
J. Phys. Chem. C 2020, 124, 25211−25220

Small modulation transient photovoltage (SMPVT) measurements were also undertaken to further probe the lifetime of electrons in TiO_2 after photoexcitation (Figure 8).[47] This

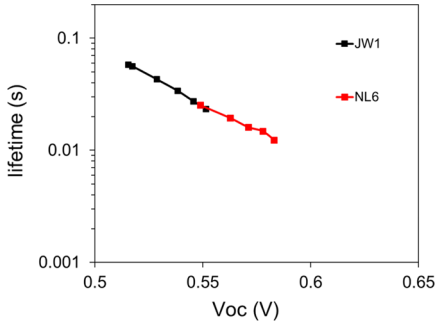

Figure 8. Small modulation photovoltage transient (SMPVT) measurements for **JW1** and **NL6**.

technique uses small light intensity changes to cause the V_{OC} values to rise or decay. The rate of this rise and decay is then fitted and attributed to the lifetime of the electron in TiO_2 after photoinduced electron transfer. Via SMPVT, **JW1** and **NL6** devices were found to have near identical electron lifetimes, which suggest similar recombination rates under these conditions. Additionally, capacitance measured under open-circuit conditions with varied potentials by light intensity reveals no significant change in the capacitance with either dye, which suggests that the changes in the V_{oc} values between the two dyes may be most closely related to recombination losses (Figure S11).[47] Although the recombination rate of electrons in the TiO_2 with the electrolyte with **NL6** devices relative to **JW1** devices is either slowed down or similar, the dramatically large photocurrent of **JW1** leads to an overall higher PCE value of 7.4% with **JW1** versus 5.4% with **NL6** under the conditions tested here (Table 3). The origin of the improved photocurrent is not obvious from these studies but is likely due to differences in either regeneration efficiencies or injection efficiencies of the two dyes. Notably, **JW1** has an approximately 100 mV higher driving force for electron injection. At reduced irradiation intensity, which is of value for indoor and diffuse lighting situations where DSCs have been record setting,[6,10] a PCE of 9.2% with **JW1** is measured at 10% sun intensity (Table 3). Importantly, the triple donor design has enabled the use of a single chromophore to collect the full visible range of photons, which can dramatically simplify device fabrication and optimization protocols. Single chromophores that give fully panchromatic DSC device responses are rare in the literature.[9] Importantly, DSC devices with **JW1** were found to be stable under continuous light-soaking conditions for up to 500 h with a less than 10% loss in PCE over this time frame (Figure 9). This result indicates the triple donor dye design is also robust under operating conditions and further suggests that this design is of practical merit.

CONCLUSIONS

A fully panchromatic dye has been realized by engineering additional cross-conjugated ICT bands into the absorption spectrum of a novel sensitizer incorporating a thienopyrazine π-bridge with a unique triple donor design and cyanoacrylic acid acceptor. Computational results illustrate the importance of each TAA donor contributing to the introduction of several

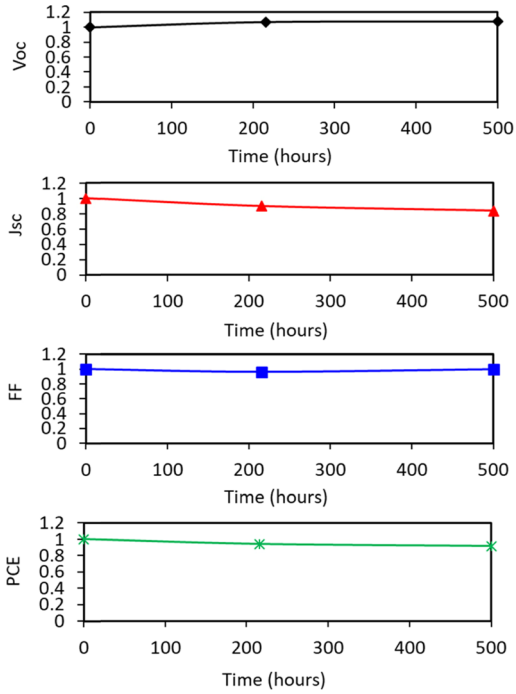

Figure 9. DSC device stability study for **JW1**. *Y* axis values are normalized.

higher energy absorption curve features relative to the lowest energy charge transfer band. Such dyes are rare in the literature, and this approach offers a molecular design strategy that can alleviate the challenges of designing and optimizing cosensitized DSC devices for a panchromatic device response. This all-in-one design led to an exceptionally high single dye photocurrent density of 19.7 mA/cm^2. Very few dyes in DSC devices based on organic chromophores have reached this value without the aid of cosensitization strategies. The design is robust during continuous light soaking studies, indicating that this approach is of practical merit for further consideration in next-generation dye designs. Future studies will focus on using this general design approach with alternative π-bridges to access higher-energy excited-state dyes. This will improve on the photovoltages observed herein through enabling the use of lower lithium loadings in the electrolyte. Additionally, this dye design is a good approach for accessing NIR chromophores for use in multijunction solar cell systems where this technology can be paired with other solar cell technologies currently being developed.

ASSOCIATED CONTENT

Supporting Information

The Supporting Information is available free of charge at https://pubs.acs.org/doi/10.1021/acs.jpcc.0c07003.

Electrochemical data, additional device data, computation information, and NMR spectra (PDF)

AUTHOR INFORMATION

Corresponding Author

Jared H. Delcamp − *Department of Chemistry and Biochemistry, Coulter Hall, University of Mississippi, University, Mississippi 38677, United States;* orcid.org/0000-0001-5313-4078; Email: delcamp@olemiss.edu

https://dx.doi.org/10.1021/acs.jpcc.0c07003
J. Phys. Chem. C 2020, 124, 25211−25220

Authors

Jonathon Watson − *Department of Chemistry and Biochemistry, Coulter Hall, University of Mississippi, University, Mississippi 38677, United States;* orcid.org/0000-0003-4307-0730

Taylor J. Santaloci − *Department of Chemistry and Biochemistry, Coulter Hall, University of Mississippi, University, Mississippi 38677, United States;* orcid.org/0000-0001-8958-2569

Hammad Cheema − *Department of Chemistry and Biochemistry, Coulter Hall, University of Mississippi, University, Mississippi 38677, United States;* orcid.org/0000-0002-7045-0141

Ryan C. Fortenberry − *Department of Chemistry and Biochemistry, Coulter Hall, University of Mississippi, University, Mississippi 38677, United States;* orcid.org/0000-0003-4716-8225

Complete contact information is available at: https://pubs.acs.org/10.1021/acs.jpcc.0c07003

Notes

The authors declare no competing financial interest.

■ ACKNOWLEDGMENTS

J.W., H.C., and J.H.D. thank the National Science Foundation (NSF) for supporting this research with award 1954922. Preliminary results were collected under NSF award 1455167. R.C.F. and T.J.S. acknowledge funding from NSF grant OIA-1757220. T.J.S. is supported by a fellowship from the Mississippi Space Grant Foundation through NASA Grant NNH19ZHA001C.

■ REFERENCES

(1) Zhang, S.; Yang, X.; Numata, Y.; Han, L. Highly Efficient Dye-Sensitized Solar Cells: Progress and Future Challenges. *Energy Environ. Sci.* **2013**, *6*, 1443−1464.

(2) Fakharuddin, A.; Jose, R.; Brown, T. M.; Fabregat-Santiago, F.; Bisquert, J. A Perspective on the Production of Dye-Sensitized Solar Modules. *Energy Environ. Sci.* **2014**, *7*, 3952−3981.

(3) Polman, A.; Knight, M.; Garnett, E. C.; Ehrler, B.; Sinke, W. C. Photovoltaic Materials: Present Efficiencies and Future Challenges. *Science* **2016**, *352*, aad4424.

(4) Saifullah, M.; Gwak, J.; Yun, J. H. Comprehensive Review on Material Requirements, Present Status, and Future Prospects for Building-Integrated Semitransparent Photovoltaics (BISTPV). *J. Mater. Chem. A* **2016**, *4*, 8512−8540.

(5) Nam, S.-H.; Lee, K. H.; Yu, J.-H.; Boo, J.-H. Review of the Development of Dyes for Dye-Sensitized Solar Cells. *Appl. Sci. Conv. Technol.* **2019**, *28*, 194−206.

(6) Cao, Y.; Liu, Y.; Zakeeruddin, S. M.; Hagfeldt, A.; Grätzel, M. Direct Contact of Selective Charge Extraction Layers Enables High-Efficiency Molecular Photovoltaics. *Joule* **2018**, *2*, 1108−1117.

(7) Hardin, B. E.; Snaith, H. J.; McGehee, M. D. The Renaissance of Dye-Sensitized Solar Cells. *Nat. Photon.* **2012**, *6*, 162−169.

(8) Brogdon, P.; Cheema, H.; Delcamp, J. H. Near-Infrared-Absorbing Metal-Free Organic, Porphyrin, and Phthalocyanine Sensitizers for Panchromatic Dye-Sensitized Solar Cells. *ChemSusChem* **2018**, *11*, 86−103.

(9) Mathew, S.; Yella, A.; Gao, P.; Humphry-Baker, R.; Curchod, B. F.; Ashari-Astani, N.; Tavernelli, I.; Rothlisberger, U.; Nazeeruddin, M. K.; Grätzel, M. Dye-Sensitized Solar Cells with 13% Efficiency Achieved through the Molecular Engineering of Porphyrin Sensitizers. *Nat. Chem.* **2014**, *6*, 242−247.

(10) Freitag, M.; Teuscher, J.; Saygili, Y.; Zhang, X.; Giordano, F.; Liska, P.; Hua, J.; Zakeeruddin, S. M.; Moser, J.-E.; Grätzel, M.; et al. Dye-Sensitized Solar Cells for Efficient Power Generation under Ambient Lighting. *Nat. Photon.* **2017**, *11*, 372−378.

(11) Kakiage, K.; Aoyama, Y.; Yano, T.; Oya, K.; Fujisawa, J. I.; Hanaya, M. Highly-Efficient Dye-Sensitized Solar Cells with Collaborative Sensitization by Silyl-Anchor and Carboxy-Anchor Dyes. *Chem. Commun.* **2015**, *51*, 15894−15897.

(12) Eom, Y. K.; Kang, S. H.; Choi, I. T.; Yoo, Y.; Kim, J.; Kim, H. K. Significant Light Absorption Enhancement by a Single Heterocyclic Unit Change in the π-Bridge Moiety from Thieno[3,2-B]Benzothiophene to Thieno[3,2-B]Indole for High Performance Dye-Sensitized and Tandem Solar Cells. *J. Mater. Chem. A* **2017**, *5*, 2297−2308.

(13) Pei, K.; Wu, Y.; Li, H.; Geng, Z.; Tian, H.; Zhu, W. H. Cosensitization of D-A-π-A Quinoxaline Organic Dye: Efficiently Filling the Absorption Valley with High Photovoltaic Efficiency. *ACS Appl. Mater. Interfaces* **2015**, *7*, 5296−5304.

(14) Liu, J.; Liu, B.; Tang, Y.; Zhang, W.; Wu, W.; Xie, Y.; Zhu, W.-H. Highly Efficient Cosensitization of D−A−π−A Benzotriazole Organic Dyes with Porphyrin for Panchromatic Dye-Sensitized Solar Cells. *J. Mater. Chem. C* **2015**, *3*, 11144−11150.

(15) Hardin, B. E.; Sellinger, A.; Moehl, T.; Humphry-Baker, R.; Moser, J. E.; Wang, P.; Zakeeruddin, S. M.; Grätzel, M.; McGehee, M. D. Energy and Hole Transfer between Dyes Attached to Titania in Cosensitized Dye-Sensitized Solar Cells. *J. Am. Chem. Soc.* **2011**, *133*, 10662−10667.

(16) Xie, Y.; Tang, Y.; Wu, W.; Wang, Y.; Liu, J.; Li, X.; Tian, H.; Zhu, W. H. Porphyrin Cosensitization for a Photovoltaic Efficiency of 11.5%: A Record for Non-Ruthenium Solar Cells Based on Iodine Electrolyte. *J. Am. Chem. Soc.* **2015**, *137*, 14055−14058.

(17) Patwari, J.; Sardar, S.; Liu, B.; Lemmens, P.; Pal, S. K. Three-in-One Approach Towards Efficient Organic Dye-Sensitized Solar Cells: Aggregation Suppression, Panchromatic Absorption and Resonance Energy Transfer. *Beilstein J. Nanotechnol.* **2017**, *8*, 1705−1713.

(18) Kakiage, K.; Aoyama, Y.; Yano, T.; Oya, K.; Kyomen, T.; Hanaya, M. Fabrication of a High-Performance Dye-Sensitized Solar Cell with 12.8% Conversion Efficiency Using Organic Silyl-Anchor Dyes. *Chem. Commun.* **2015**, *51*, 6315−6317.

(19) Kuang, D.; Walter, P.; Nüesch, F.; Kim, S.; Ko, J.; Comte, P.; Zakeeruddin, S. M.; Nazeeruddin, M. K.; Grätzel, M. Co-Sensitization of Organic Dyes for Efficient Ionic Liquid Electrolyte-Based Dye-Sensitized Solar Cells. *Langmuir* **2007**, *23*, 10906−10909.

(20) Cooper, C. B.; Beard, E. J.; Vázquez-Mayagoitia, Á.; Stan, L.; Stenning, G. B. G.; Nye, D. W.; Vigil, J. A.; Tomar, T.; Jia, J.; Bodedla, G. B.; et al. Design-to-Device Approach Affords Panchromatic Co-Sensitized Solar Cells. *Adv. Energy Mater.* **2019**, *9*, 1802820.

(21) Cole, J. M.; Pepe, G.; Al Bahri, O. K.; Cooper, C. B. Cosensitization in Dye-Sensitized Solar Cells. *Chem. Rev.* **2019**, *119*, 7279−7327.

(22) Zeng, K.; Chen, Y.; Zhu, W. H.; Tian, H.; Xie, Y. Efficient Solar Cells Based on Concerted Companion Dyes Containing Two Complementary Components: An Alternative Approach for Cosensitization. *J. Am. Chem. Soc.* **2020**, *142*, 5154−5161.

(23) Fan, S.; Lu, X.; Sun, H.; Zhou, G.; Chang, Y. J.; Wang, Z. S. Effect of the Co-Sensitization Sequence on the Performance of Dye-Sensitized Solar Cells with Porphyrin and Organic Dyes. *Phys. Chem. Chem. Phys.* **2016**, *18*, 932−938.

(24) Lu, X.; Zhou, G.; Wang, H.; Feng, Q.; Wang, Z. S. Near Infrared Thieno[3,4-B]Pyrazine Sensitizers for Efficient Quasi-Solid-State Dye-Sensitized Solar Cells. *Phys. Chem. Chem. Phys.* **2012**, *14*, 4802−4809.

(25) Bourass, M.; Fitri, A.; Benjelloun, M.; Mcharfi, M.; Hamidi, M.; Serein-Spirau, F.; Jarrosson, T.; Lere-Porte, J. P.; Sotiropoulos, J. M.; Bouachrine, M. DFT and TDDFT Investigations of New Thienopyrazine-Based Dyes for Solar Cells: Effects of Electron Donor Groups. *Der. Pharm. Chem.* **2013**, *5*, 144−153.

(26) Liyanage, N. P.; Cheema, H.; Baumann, A. R.; Zylstra, A. R.; Delcamp, J. H. Effect of Donor Strength and Bulk on Thieno[3,4-B]-Pyrazine-Based Panchromatic Dyes in Dye-Sensitized Solar Cells. *ChemSusChem* **2017**, *10*, 2635−2641.

(27) Wu, J.; Li, G.; Zhang, L.; Zhou, G.; Wang, Z.-S. Energy Level Engineering of Thieno[3,4-B]Pyrazine Based Organic Sensitizers for Quasi-Solid-State Dye-Sensitized Solar Cells. *J. Mater. Chem. A* **2016**, *4*, 3342−3355.
(28) Liyanage, N. P.; Yella, A.; Nazeeruddin, M.; Grätzel, M.; Delcamp, J. H. Thieno[3,4-B]Pyrazine as an Electron Deficient π-Bridge in D-A-π-A DSCs. *ACS Appl. Mater. Interfaces* **2016**, *8*, 5376−5384.
(29) Paredes-Gil, K.; Páez-Hernández, D.; Arratia-Pérez, R.; Mendizábal, F. Insights into the Role of D-A-π-A Type Pro-Aromatic Organic Dyes with Thieno[3,4-B]Pyrazine as a Acceptor Group into Dye-Sensitized Solar-Cells. A TD-DFT/Periodic DFT Study. *Int. J. Quantum Chem.* **2020**, *120*, No. e26108.
(30) Delcamp, J. H.; Shi, Y.; Yum, J. H.; Sajoto, T.; Dell'Orto, E.; Barlow, S.; Nazeeruddin, M. K.; Marder, S. R.; Grätzel, M. The Role of π-Bridges in High-Efficiency DSCs Based on Unsymmetrical Squaraines. *Chem. − Eur. J.* **2013**, *19*, 1819−1827.
(31) Schwiderski, R. L.; Rasmussen, S. C. Synthesis and Characterization of Thieno[3,4-B]Pyrazine-Based Terthienyls: Tunable Precursors for Low Band Gap Conjugated Materials. *J. Org. Chem.* **2013**, *78*, 5453−5462.
(32) Nietfeld, J. P.; Schwiderski, R. L.; Gonnella, T. P.; Rasmussen, S. C. Structural Effects on the Electronic Properties of Extended Fused-Ring Thieno[3,4-B]Pyrazine Analogues. *J. Org. Chem.* **2011**, *76*, 6383−6388.
(33) McNamara, L. E.; Liyanage, N.; Peddapuram, A.; Murphy, J. S.; Delcamp, J. H.; Hammer, N. I. Donor-Acceptor-Donor Thienopyrazines Via Pd-Catalyzed C-H Activation as NIR Fluorescent Materials. *J. Org. Chem.* **2015**, *81*, 32−42.
(34) Mátravölgyi, B.; Hergert, T.; Thurner, A.; Varga, B.; Sangiorgi, N.; Bendoni, R.; Zani, L.; Reginato, G.; Calamante, M.; Sinicropi, A.; et al. Synthesis and Investigation of Solar-Cell Photosensitizers Having a Fluorazone Backbone. *Eur. J. Org. Chem.* **2017**, *2017*, 1843−1854.
(35) Lee, C.; Yang, W.; Parr, R. G. Development of the Colle-Salvetti Correlation-Energy Formula into a Functional of the Electron Density. *Phys. Rev. B* **1988**, *37*, 785−789.
(36) Becke, A. D. Density-Functional Thermochemistry. III. The Role of Exact Exchange. *J. Chem. Phys.* **1993**, *98*, 5648−5652.
(37) Frisch, M. J.; Pople, J. A.; Binkley, J. S. Self-Consistent Molecular Orbital Methods 25. Supplementary Functions for Gaussian Basis Sets. *J. Chem. Phys.* **1984**, *80*, 3265−3269.
(38) Frisch, M. J.; Trucks, G. W.; Schlegel, H. B.; Scurseria, G. E.; Robb, M. A.; Cheeseman, J. R.; Scalmani, G.; Barone, V.; Mennucci, B.; Petersson, A.; et al. *Gaussian09 Revision E.01*. Gaussian, Inc. 2009, Wallingford, CT, USA.
(39) Sun, Z.; Liang, M.; Chen, J. Kinetics of Iodine-Free Redox Shuttles in Dye-Sensitized Solar Cells: Interfacial Recombination and Dye Regeneration. *Acc. Chem. Res.* **2015**, *48*, 1541−1550.
(40) Pashaei, B.; Shahroosvand, H.; Abbasi, P. Transition Metal Complex Redox Shuttles for Dye-Sensitized Solar Cells. *RSC Adv.* **2015**, *5*, 94814−94848.
(41) Hagfeldt, A.; Boschloo, G.; Sun, L.; Kloo, L.; Pettersson, H. Dye-Sensitized Solar Cells. *Chem. Rev.* **2010**, *110*, 6595−6663.
(42) Anderson, A. Y.; Barnes, P. R. F.; Durrant, J. R.; O'Regan, B. C. Quantifying Regeneration in Dye-Sensitized Solar Cells. *J. Phys. Chem. C* **2010**, *115*, 2439−2447.
(43) Boschloo, G.; Hagfeldt, A. Characteristics of the Iodide/Triiodide Redox Mediator in Dye-Sensitized Solar Cells. *Acc. Chem. Res.* **2009**, *42*, 1819−1826.
(44) Ardo, S.; Meyer, G. J. Photodriven Heterogeneous Charge Transfer with Transition-Metal Compounds Anchored to TiO_2 Semiconductor Surfaces. *Chem. Soc. Rev.* **2009**, *38*, 115−164.
(45) Urbani, M.; Grätzel, M.; Nazeeruddin, M. K.; Torres, T. Meso-Substituted Porphyrins for Dye-Sensitized Solar Cells. *Chem. Rev.* **2014**, *114*, 12330−12396.
(46) Mishra, A.; Fischer, M. K.; Bauerle, P. Metal-Free Organic Dyes for Dye-Sensitized Solar Cells: From Structure: Property Relationships to Design Rules. *Angew. Chem., Int. Ed.* **2009**, *48*, 2474−2499.
(47) Boschloo, G.; Häggman, L.; Hagfeldt, A. Quantification of the Effect of 4-Tert-Butylpyridine Addition to I^-/I_3^- Redox Electrolytes in Dye-Sensitized Nanostructured TiO_2 Solar Cells. *J. Phys. Chem. B* **2006**, *110*, 13144−13150.

https://dx.doi.org/10.1021/acs.jpcc.0c07003
J. Phys. Chem. C 2020, 124, 25211−25220